Investigation of spontaneous imbibition behavior in a 3D pore space under reservoir condition by muti-component pseudo-potential lattice Boltzmann method

Jiangtao Zheng[1], Wenhai Lei[2], Yang Ju[1,3], and Moran Wang[2, †]

[1]State Key Laboratory of Coal Resources and Safe Mining, China University of Mining & Technology, Beijing, China.

[2]Department of Engineering Mechanics, School of Aerospace, Tsinghua University, Beijing, China.

[3]State Key Laboratory for Geomechanics and Deep Underground Engineering, China University of Mining & Technology, Xuzhou, China.

Corresponding author: Moran Wang (mrwang@tsinghua.edu.cn); Yang Ju (juy@cumtb.edu.cn);

Key Points:

- Direct pore-scale simulation of spontaneous imbibition in a 3D pore space extracted from a tight reservoir rock.
- Spontaneous imbibition under reservoir condition is about two times faster than that under ambient condition due to lower viscous force.
- Snap-off of oil droplets during the SI mainly occurred in pore bodies surrounded by slit-shaped pore throats.

† Corresponding author; Email address: mrwang@tsinghua.edu.cn

Abstract

Spontaneous imbibition of the injected fluid into the pore space of a tight oil reservoir and replacing the crude oil therein has been considered as one of the possible mechanisms in increasing oil recovery. Such deeply buried reservoir rocks is usually under high-pressure and high-temperature conditions. Besides, their interior complex porous structures are usually characterized as pore bodies and slit-shaped pore throats. As a result, an accurate description of the spontaneous imbibition behavior driven by capillary force in the real pore space under reservoir conditions is crucial to understand the process and uncover the controlling mechanisms. An improved multi-component pseudo-potential lattice Boltzmann method was developed to simulate the spontaneous imbibition behavior in a representative 3D pore space extracted from a tight sandstone reservoir rock. Comparison of the spontaneous imbibition behavior under ambient condition and reservoir condition showed that the latter case exhibited two times faster of the imbibition. Moreover, a snap-off of the oil droplet phenomenon was observed in the pore bodies surrounded by slit-shaped pore throats. The snap-off oil droplets stuck in the pore bodies and accounted for 9.47 % of the pore volume. These results indicated the importance of investigating the spontaneous imbibition in a real porous structure and under actual reservoir condition. The proposed pore-scale simulation method provides a useful tool in understanding the complex spontaneous imbibition pattern and the resulted enhanced oil recovery.

Plain Language Summary

Tight oil reservoir has become an important world energy supply due to formation stimulations such as hydraulic fracturing. In the process, a large amount of water was injected and retained in the formation. It is believed that the capillary force induced spontaneous imbibition of the residual water into the tiny pore space is beneficial to the oil recovery in the tight reservoir. However, an accurate description of the process that happened deep underground is difficult and the controlling mechanism remains to be fully understood. Here, pore-scale simulations were performed to directly visualize the detailed spontaneous imbibition behavior under the reservoir and ambient conditions. The results showed (1) faster spontaneous imbibition appeared under the reservoir condition, (2) snap-off of the oil droplets occurred in the pore bodies. These findings suggest that the reservoir temperature and pressure and the detailed pore morphology have a huge impact on the spontaneous imbibition behavior.

1 Introduction

Unconventional oil reservoirs, which are previously classified as uneconomic resources by traditional developing methods, have become one of the important world energy supplying parts in recent years with the application of horizontal drilling, hydraulic fracturing and numerous enhanced oil recovery (EOR) methods (K. Singh et al., 2019; Xie et al., 2021). These oil reservoirs usually bury deep underground with conditions characterized as high-pressure and high-temperature. In a typical unconventional oil reservoir exploitation, a hydraulic fracturing job is proceeded after the completion of horizontal drilling to increase transport channels for oil recovery (Z. Chen et al., 2020). Previously, a flowback operation of the fracturing fluid is usually designed to decrease the potential reservoir damage. However, recent developments in these oil fields showed that partly flowback or even no flowback with the subsequent shut-in operation increased the oil recovery (Abbasi et al., 2014; Bertoncello et al., 2014; J. Liu et al., 2019).

Spontaneous imbibition (SI) of the injected fluid into the reservoir pore space and displacement of the crude oil therein are claimed as one of the principal reasons for the increased oil recovery in the unconventional reservoir during the shut-in operation (K. Singh et al., 2019). The SI is a particular type of multiphase flow driven by capillary force. For a typical tight rock, the characteristic radius of its pore space is usually very small, which ranges from tens nanometers to tens micrometers (Lai et al., 2018; Nelson, 2009). According to the Young and Laplace equation, capillary force becomes one of the dominant factors that control the flow in such a small-scale porous media. Based on whether the flow directions of imbibed-in wetting phase and driven-out non-wetting phase are the same or opposite, the SI is classified as co-current SI and counter-current SI. In a hydrophilic tight reservoir rock, the SI of the injected aqueous fluid would cause the oil replacing in the pore space.

Several core scale laboratory studies have verified the potential of increasing oil recovery by SI (Abbasi et al., 2014; Bertoncello et al., 2014; Habibi et al., 2015; H. Singh, 2016). For instance, nuclear magnetic resonance (NMR) was used to investigate the SI in tight rocks (Cheng et al., 2018; Wang et al., 2018) and the results showed that distinct recovery performance was observed in different pore sizes. Lan et al. (2015) compared the SI in intact and crushed samples of tight rocks and argued that rock fabric and pore connectivity played a crucial role in the SI behavior. Haugen et al. (2014) pointed out co-current SI was more important than counter-current SI for oil recovery. Moreover, adding surfactant or nanoparticles in the imbibed fluid was argued to be beneficial to the oil recovery (Dai et al., 2017; Mohammadi et al., 2019). For instance, Xu et al. (2019) investigated the contribution of interfacial tension (IFT) reduction and wettability alteration on EOR separately during the SI and pointed out ultra-low IFT and increasing the hydrophilicity of the sample were desirable for the EOR. Hodder et al. (Hodder & Nychka, 2019) investigated the influence of wettability on the SI behavior in 3D printed sandstone samples. Besides, the reservoir temperature and pressure have non-negligible influences on the in-situ fluid properties such as viscosity and interfacial tension (Kalantari Meybodi et al., 2016; Strand et al., 2008; S. Yang, 2017; Zeppieri et al., 2001). An accurate description of the SI behavior was complicated due to the geometrical complexity of the porous structure and the in-situ high-pressure and high-temperature conditions. There is not a consensus on the relative importance of the influence factors based on the core scale experiments (Kibria et al., 2018; Kuang et al., 2020). A detailed investigation of the SI in the pore-scale at reservoir conditions is crucial in uncovering the controlling mechanisms of fluids imbibed-in and driven-out from the rock.

Several pore-scale theoretical models, experiments, and simulations have been conducted to accurately describe the SI behavior. Such an investigation of the detailed pore-scale SI behavior under reservoir conditions are necessary to unveil the complex flow dynamics in the unconventional reservoir. The classical Lucas-Washburn (LW) equation, which can be dated back to the early 20th century, stated that the SI length in a capillary tube is proportional to $\sqrt{t}$ (Washburn, 1921). However, actual pore geometry in tight rocks is far from a collection of cylindrical tubes and the applicability of LW law can be questioned (Ponomarenko et al., 2011). Reyssat et al. (Reyssat et al., 2008) demonstrated the SI behavior in channels with axial variations followed $l \propto \sqrt{t}$ at short times, whereas $l \propto \sqrt[4]{t}$ at longer times. They also argued SI rate in porous media will depend on the spatial variation of the permeability. Ponomarenko et al. (Ponomarenko et al., 2011) indicated that the capillary rise in corners of irregular pores followed $l \propto \sqrt[3]{t}$. Primkulov et al. (Primkulov et al., 2020) stated that a large fraction of dispassion happened near the contact line and dynamic contact angle should be used for the accurate descriptions of the SI behavior. A recent review of LW law based modeling of the SI was presented by Cai et al (Cai et al., 2021). Although it was found that the SI in a homogeneous porous media obeyed the LW law, the pore space in an unconventional tight reservoir rock showed much more heterogeneity and geometrical irregularity. Whether the LW law still applicable needs to be further investigated (H. Singh, 2016; Wang et al., 2018; R. Yang et al., 2017).

Developments in the visualization of pore-scale multiphase flow behavior were facilitated by accurate fabrication of micromodels and fast development of imaging methods. The visualization of the detailed SI processes in delicate 2D transparent models enabled several new discoveries of the transport mechanisms (Zhang et al., 2011; B. Zhao et al., 2016; Zheng et al.,

2021). For instance, the SI in glass beads models showed that the pore size distribution played significant roles in the propagation pattern (Ashraf et al., 2017) and the residual oil distribution (Hatiboglu & Babadagli, 2008; Meng et al., 2016). The micromodel with structural details of the actual pore space in a rock was used to study the pore-level physics of the SI (Meng et al., 2016; Sun et al., 2016). It was found the pore geometry has a non-negligible influence on the imbibition morphology. The fast development of 3D imaging methods, such as magnetic resonance imaging (MRI) and X-ray computer tomography (CT), enabled the direct observation of the SI inside reservoir rock samples (Armstrong et al., 2014; Bazaikin et al., 2017; David et al., 2011; Fernø et al., 2013). For instance, Fernø et al. (Fernø et al., 2013) visualized the details of SI front by MRI and pointed out that the core heterogeneities had a dominant effect on the SI behavior. Zhao et al. (Y. Zhao et al., 2017) employed the CT and neutron radiography to characterize the influence of pore structure on the water imbibition in tight sandstones. Moreover, the 3D images of the flow evolution inside a rock sample have been reported by using high spatial and temporal resolution CT (Alhammadi et al., 2020; Alzahid et al., 2020; Gao et al., 2020; Iglauer & Lebedev, 2018; Joyce et al., 2015; Ju et al., 2018). Singh et al.(Kamaljit Singh et al., 2017) captured the snap-off process during imbibition using fast synchrotron X-ray CT and stated the process was favorable for a large aspect ratio of local pores. Kuang et al.(Kuang et al., 2020) argued that wettability reversal after SI of the nanofluids was the main mechanism based on the direct contact angle measurement in the pore space. The recent advent of in situ-CT has made it possible to directly image the rock and fluid distribution within the pores at the reservoir temperature and pressure (AlRatrout et al., 2018). However, such an experiment is expensive and the temporal resolution is insufficient to capture the detailed dynamic process during the SI.

Several simulation methods facilitated the investigation of multiphase flow dynamics in complex porous structures, such as computational fluid dynamics modeling (Jafari et al., 2017), pore network modeling (Valvatne & Blunt, 2004), and lattice Boltzmann method (LBM) (Ju et al., 2020; Li et al., 2016). Among them, the LBM, which is built upon the mesoscopic kinetic equations, stands out for modeling cases with complex boundary conditions and multiphase interfaces (S. Chen & Gary, 1998). Such direct pore-scale simulations of the SI in 3D porous structures enable one to capture the distinct influence of 3D pore morphology, pore surface wettability, and fluid properties on the imbibition dynamics. There are four basic multiphase LBMs, which include the color gradient model, the pseudo-potential lattice Boltzmann method (SC-LBM), the free-energy model, and the phase-field model (Aidun & Clausen, 2010). Liu et al. (Y. Liu et al., 2020) simulated the counter-current SI by the color gradient LBM and indicated the micro-fractures improved the oil recovery. Bakhshian et al. (Bakhshian et al., 2020) investigated the SI dynamics in fractured rock samples and argued the complex pore space geometries led to a non-uniform advancement of the interface. Zacharoudiou et al. (Zacharoudiou et al., 2017) simulated the two-phase flow dynamics in micro-fluidics by the free energy LBM and compared it with the experimental results. Liu et al. (H. Liu & Zhang, 2016) simulated the dynamic behavior of a confined droplet by the phase-field LBM. Zheng et al. (Zheng, Chen, et al., 2018; Zheng, Ju, et al., 2018) employed the single component multi-phase SC-LBM to investigate the interface dynamics and the SI behavior in complex 3D porous structure. The above mentioned numerical methods provide suitable tools to quantitatively describe the SI behavior at the pore-scale. Among them, the SC-LBM has become one of the most popular multiphase flow methods due to its easy implementation.

166 There is no doubt investigations of the flow dynamics at pore-scale and under reservoir
167 condition are crucial to uncovering the controlling mechanisms of the complex SI behavior in
168 unconventional rocks. During the shut-in operation, the SI of the fracturing fluid takes place in
169 the complex pore space of the reservoir rock and faces high temperature and pressure conditions.
170 In this work, we employed the multi-component SC-LBM to investigate detailed SI behavior in
171 the porous structure of a tight sandstone sample. The micro-CT scanning was first used to obtain
172 a high-resolution 3D image of the rock sample. Then image processing technics were employed
173 to extract the 3D porous structure. An improved multi-component SC-LBM was developed to
174 investigate the SI therein. The SI under ambient and reservoir conditions were calculated and
175 compared. Moreover, the detailed snap-off of oil droplet was analyzed.

176 **2 Materials and Methods**

177 2.1 Porous structure of a tight reservoir sandstone

178 The Changqing oil field is mainly characterized as a low-permeability tight reservoir with
179 an average temperature of 80 ℃ and pressure of 15 MPa (S. Yang, 2017). Moreover, the
180 reservoir usually has high oil saturation. The viscosity of the in-situ crude oil is around 1 mPa·s.

181 In order to investigate pore-scale SI behavior in a tight reservoir, a 3D porous structure of
182 a tight reservoir rock sample was first imaged by a micro-CT scanner (Sanying, China). The
183 sample was drilled from Changqing oilfield (China) and characterized as a low-permeability
184 tight sandstone. Totally, 1258 slices with an image size of 1,630 × 1,630 pixels were
185 reconstructed from the scanning data. The reconstructed 3D grayscale image, as shown in Figure
186 1(a), has a voxel resolution of 0.772 μm. A middle slice image of the sample is shown in Figure
187 1(b). As observed, the sample is composed of granular particles and irregular high aspect ratio

188 interparticle pores. The pore bodies mainly connect with each other through slit-shaped pore
189 throats.

190 Several image processing procedures were applied to extract the porous structure from
191 the reconstructed 3D image. First, a central 800^3 cubic region was selected for further
192 processing, as illustrated in the middle slice by a yellow box in Figure 1(b). Then the non-local
193 mean denoising algorithm (Buades et al., 2005) was employed to decrease the image noise.
194 Moreover, a Hessian-based filtering technique (Voorn et al., 2013), which providing an efficient
195 way for better extracting the slit-shaped pores, was used in the image segmentation process. It
196 should be noted that a conventional global segmentation method is hard to preserve accurate
197 information of the slit-shaped pore throats. The middle slice of the segmented binary model is
198 shown in Figure 1(c) with a comparison of the region in the yellow box in Figure 1(b). The pore
199 size distribution was calculated based on the binary model (Blunt et al., 2013; Dong & Blunt,
200 2009), which showed a quick decreasing trend as the pore size increase, as shown in Figure 1(d).
201 The calculated mean pore radius is 4.462 μm. The model was further compressed to a 100^3 cubic
202 for the efficiency of the SC-LBM simulation, as shown in Figure 1(e).

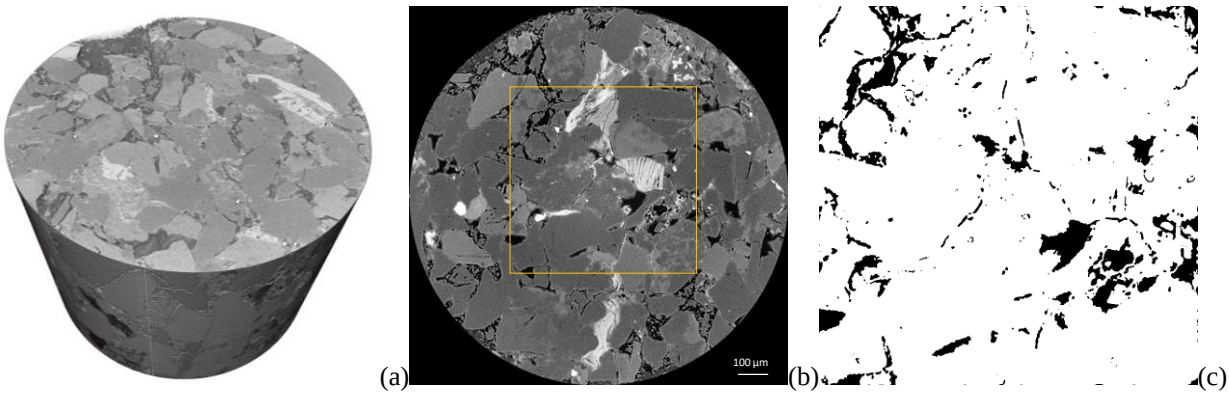

203 (a) (b) (c)

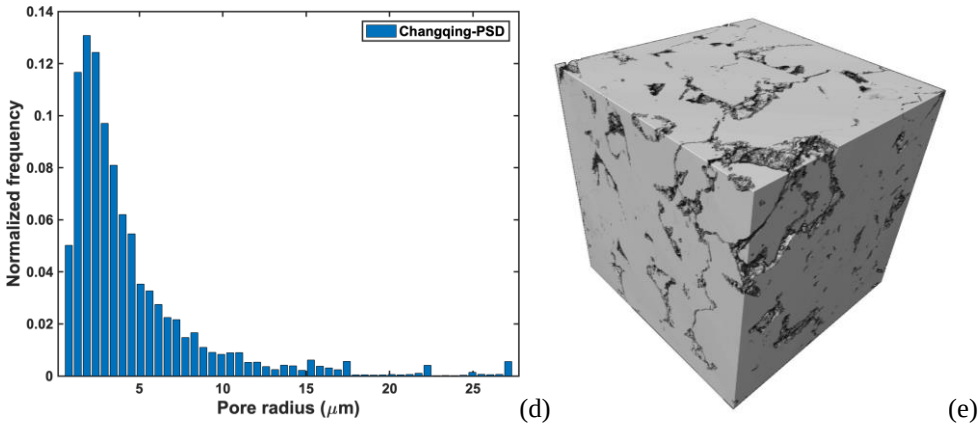

(d) (e)

Figure. 1. The porous structure of a tight reservoir sandstone. (a) Reconstructed 3D grayscale image based on the CT scan data, (b) a 2D slice in the middle of the sample, (c) middle slice of the segmented binary model, (d) pore size distribution of the sample, (e) compressed 3D model for the SI simulation.

2.2 Multi-component SC-LBM

An improved multi-component SC-LBM, with modification of the interaction force between fluids and solids, was employed to simulate the SI behavior in the porous model. The D3Q19 square lattice with explicit forcing terms and multiple relaxation time method (MRT) was used and the general framework of the model is similar to previous work (Coon et al., 2014; Porter et al., 2012). For completeness, we briefly introduce the main framework of the model with an emphasis on the improved fluids and solids interaction forces. In the mesoscopic SC-LBM, *k* particle distribution functions are introduced to represent the multi-component fluids. The distribution function is evolved using the discrete Boltzmann equation

$$f_\alpha^k(\boldsymbol{x}+\boldsymbol{e}_\alpha\Delta t, t+\Delta t) - f_\alpha^k(\boldsymbol{x},t) = \Omega_{\text{coll}}^k + \Omega_{\text{forces}}^k \quad (1)$$

where $f_\alpha^k(\boldsymbol{x},t)$ is the density distribution function of the kth component in the αth direction and it streams on the lattice sites $\boldsymbol{x}$ at time t with fixed 19 directional velocities $\boldsymbol{e}_\alpha$. The left-hand side describes the streaming step of the distribution functions and the right-hand side discribes

the momentum change in the distribution functions due to collision (Ω^k_{coll}), and other forces (Ω^k_{forces}). The collision operator is defined as

$$\Omega^k_{\text{coll}} = M^{-1}\Lambda^k M\left[f_\alpha^{\text{eq},k}(\boldsymbol{x},t) - f_\alpha^k(\boldsymbol{x},t)\right] \quad (2)$$

where M is the transformation matrix (d'Humières, 2002) that maps the distribution function to its moments, Λ^k is diagonal relaxation matrix and defined as $\text{diag}[s_c^k, s_e^k, s_\varepsilon^k, s_c^k, s_q^k, s_c^k, s_q^k, s_c^k, s_q^k, s_\nu^k, s_\pi^k, s_\nu^k, s_\nu^k, s_\nu^k, s_\nu^k, s_\nu^k, s_m^k, s_m^k, s_m^k]$. In this study, we chose $s_c^k = 1, s_e^k = 0.1, s_\varepsilon^k = 0.1, s_q^k = 1.6, s_\pi^k = 1.4, s_m^k = 1.98$ with k = 1 and 2 (Wu et al., 2018). s_ν^k is related with the kinematic viscosity as $v^k = \frac{c^2}{3}\Delta t(\frac{1}{s_\nu^k} - 0.5)$. $f_\alpha^{\text{eq},k}$ is the equilibrium distribution function and expressed as follows

$$f_\alpha^{\text{eq},k}(\boldsymbol{x},t) = w_\alpha \rho^k(\boldsymbol{x},t)[1 + 3\frac{\boldsymbol{e}_\alpha \cdot \boldsymbol{u}^{\text{eq}}}{c^2} + 9\frac{(\boldsymbol{e}_\alpha \cdot \boldsymbol{u}^{\text{eq}})^2}{2c^2} - 3\frac{(\boldsymbol{u}^{\text{eq}})^2}{2c^2}] \quad (3)$$

where w_α=1/3 (α=0), w_α=1/18 (α=1–6), and w_α=1/36 (α=7–18). ρ^k is the macroscopic fluid density. $c = \Delta x/\Delta t$ is the ratio of lattice spacing Δx and time step Δt. $\boldsymbol{u}^{\text{eq}}$ is effective velocity, which has the same expression as total velocity $\boldsymbol{u}$, when $s_c^k = 1$ with k = 1 and 2.

The forcing operater on the right hand of Eq. 1 is defined as

$$\Omega^k_{\text{forces}} = \frac{\Delta t}{2}[f_\alpha^{F,k}(\boldsymbol{x} + \boldsymbol{e}_\alpha\Delta t, t + \Delta t) - f_\alpha^{F,k}(\boldsymbol{x},t)] \quad (4)$$

where

$$f_\alpha^{F,k} = \frac{3\boldsymbol{F}^k \cdot (\mathbf{e}_i - \mathbf{u}^{\text{eq}})}{\rho^k c^2} f_i^{\text{eq},k}$$

5)

234 A transformation $\overline{f}_{\alpha}^{k} = f_{\alpha}^{k} - \frac{\Delta t}{2} f_{\alpha}^{F,k}$ (Coon et al., 2014) is applied to Eq. (1) to yield an

235 explicit expression as

$$\overline{f}_{\alpha}^{k}(\mathbf{x} + \mathbf{e}_i \Delta t, t + \Delta t) - \overline{f}_{\alpha}^{k}(\mathbf{x}, t) = M^{-1} \Lambda^{k} M^{k} [f_{\alpha}^{\mathrm{eq},k}(\mathbf{x}, t) - \overline{f}_{\alpha}^{k}(\mathbf{x}, t) - \frac{\Delta t}{2} f_{\alpha}^{F,k}] + \Delta t f_{\alpha}^{F,k} \tag{6}$$

236 The macroscopic properties for density, momentum, and total velocity are defined as

237 follows

$$\rho^{k} = \sum_{\alpha} \overline{f}_{\alpha}^{k} \tag{7}$$

$$\rho^{k} \mathbf{u}^{k} = \sum_{\alpha} \overline{f}_{\alpha}^{k} \boldsymbol{e}_{\alpha} + \frac{\Delta t}{2} \boldsymbol{F}^{k} \tag{8}$$

$$\boldsymbol{u} = \frac{\sum_{k} \rho^{k} \mathbf{u}^{k}}{\sum_{k} \rho^{k}} \tag{9}$$

238 The forcing terms $\boldsymbol{F}^{k}$ used in this work mainly include fluid-fluid inter-particle forces

239 $\boldsymbol{F}_{\mathrm{int}}^{k}$ and the fluid-solid adhesive forces $\boldsymbol{F}_{\mathrm{ads}}^{k}$, which control the surface tension and pore surface

240 wettability in the simulation, respectively.

241 For the $\boldsymbol{F}_{\mathrm{int}}^{k}$ we only consider the interaction between different components which is

242 defined as

$$\boldsymbol{F}_{\mathrm{int}}^{k}(\boldsymbol{x}, t) = -G \rho^{k}(\boldsymbol{x}, t) \sum\nolimits_{\alpha} w_{\alpha} \rho^{\bar{k}}(\boldsymbol{x} + \boldsymbol{e}_{\alpha} \Delta t, t) \boldsymbol{e}_{\alpha} \tag{10}$$

where G controls the strength of inter-particle forces and a large value of G permits the formation of an interface between different components. It should be noted, the multicomponent SC-LBM results in partially miscible fluids with each fluid node occupied by 1 and 2 components. For each fluid node away from the interface, one component is dominant (ρ_B) and the other is considered as a dissolved minor component (ρ_S). A larger value of G corresponds to larger surface tension and lower miscibility of the binary mixture. As presented by Porter et al. (Porter et al., 2012), the surface tension obtained from 2D calculations with the explicit forcing term showed a quadratic relationship with the interaction strength. In addition, the obtained surface tension was independent of the viscosities of the components with the explicit forcing term. Here we calculated the surface tension with different values of G in a 3D domain. In each calculation, a spherical droplet of component 1 with initial radius R ranges from 25 to 35 lattices was placed in the center of a $101 \times 101 \times 101$ lattice domain. After reached equilibrium, the droplet radius r and the pressure difference ΔP between the inside and outside the droplet were calculated. According to the Laplace law for a 3D case, i.e. $\Delta P/2 = \sigma/r$, the $\Delta P/2$ should have a linear relationship with $1/r$. As shown in Figure 2, the calculated results agree well with the Laplace law.

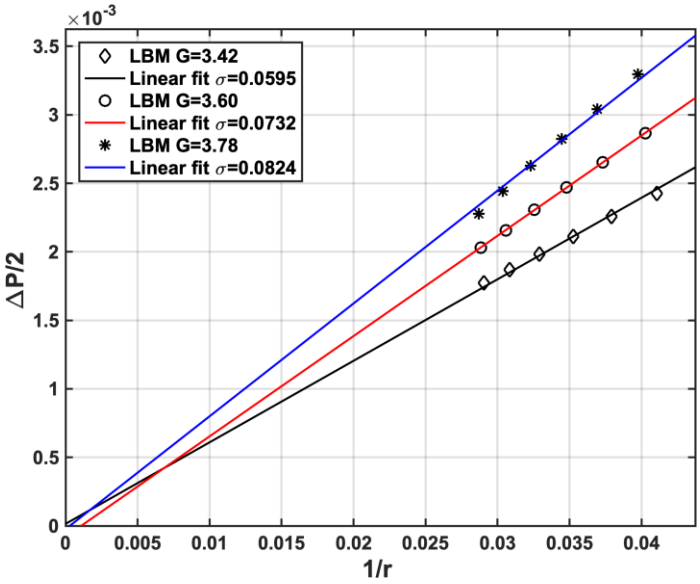

Figure. 2. Calculation of the surface tension with different values of G. The lines represent the least-square-fit of the simulation results.

Several studies have investigated the fluid-solid adhesive force $\boldsymbol{F}_{\text{ads}}^{k}$ and its relation with the contact angle (L. Chen et al., 2014; Huang et al., 2007; Kamali et al., 2011; Porter et al., 2012). In general, the $\boldsymbol{F}_{\text{ads}}^{k}$ was calculated through setting a constant fictitious wall density or a constant interaction strength between fluid and solid nodes. Such a procedure was easy to implement but would lead to unphysical density accumulation near the solid nodes especially in a capillary force dominated SI simulation (De Maio et al., 2011).

In our previous works (Zheng, Chen, et al., 2018; Zheng, Ju, et al., 2018), we proposed a modified fluid-solid interaction for single component multiphase SC-LBM, which considers the fictitious wall density as a variable rather than a constant. Here, a modified $\boldsymbol{F}_{\text{ads}}^{k}$ is employed to better control the fluid density accumulation in the multi-component SC-LBM. The basic idea is to eliminate the density accumulation near the solid nodes by controlling the interaction forces between the fluid and solid nodes. The $\boldsymbol{F}_{\text{ads}}^{k}$ is defined as

$$\boldsymbol{F}_{\mathrm{ads}}^{k}(\boldsymbol{x},t) = -G\rho^{k}(\boldsymbol{x},t)\sum_{\alpha} w_{\alpha}\rho_{w}^{\bar{k}}S(\boldsymbol{x}+\boldsymbol{e}_{\alpha}\Delta t,t)\boldsymbol{e}_{\alpha} \quad (11)$$

where $S(\boldsymbol{x}+\mathbf{e}_{\alpha}\Delta t,t)$ is an index function, which equals 1 for the solid nodes and 0 for the fluid nodes. The $\rho_{w}^{\bar{k}}$ is the fictitious wall density of the $\bar{k}$th component and its value is correlated with the average density of its 26 neighboring kth fluid density ($\overline{\rho^{k}}$). When $\overline{\rho^{k}} < 2\rho_{\mathrm{S}}$ the value of $\rho_{w}^{\bar{k}}$ is set as ρ_{B}. Otherwise the value of $\rho_{w}^{\bar{k}}$ is set as β. Similarly, the value of ρ_{w}^{k} is determined by the average density of its 26 neighboring $\bar{k}$th fluid density ($\overline{\rho^{\bar{k}}}$). When $\overline{\rho^{\bar{k}}} < 2\rho_{\mathrm{S}}$ the value of ρ_{w}^{k} is set as ρ_{B}. Otherwise, the value of ρ_{w}^{k} is set as ρ_{S}. With different values of β, a contact angle ranges from nearly 0° to 180° can be accomplished.

Considering that the real pore surface is represented by zigzag lattice nodes, as shown in Figure 1(e), we evaluated the contact angles with different values of β on a stair-shaped rough surface. The squared calculation domain has a size of $\mathrm{N_x} \times \mathrm{N_y} \times \mathrm{N_z} = 100 \times 1 \times 100$ lattices, which was divided by a diagonal line with the bottom-left region set as solid nodes and the up-right region set as fluids nodes. In each calculation, a semicircle droplet with a radius of 15 lattices of component 1 was initialized on the rough surface and the other fluid nodes initialized as component 2. The contact angle was calculated based on the interface profile after equilibrium. As shown in Figure 3, contact angles from 7.67° to 174.18° can be obtained with β values from -0.22 to 0.70.

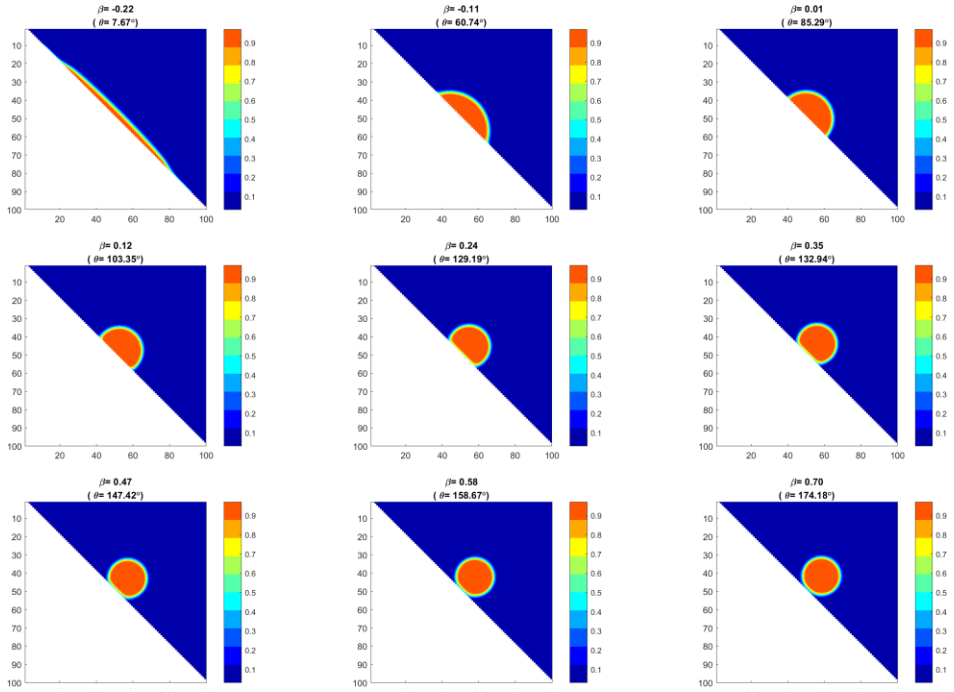

Figure. 3. Calculation of the contact angle with different values of β.

2.3 Validation of SI in a straight channel

Considering a horizontal straight plate channel initially filled with the non-wetting phase, the SI naturally happened when exposing one end of the channel into the wetting phase. The process can be considered as quasi-static state with force balance between the capillary force and viscous force except for the very short early stage (Fries & Dreyer, 2009). Such a balance can be described by the following equation

$$\frac{2\sigma\cos\theta_a}{H} = \frac{12(\mathrm{d}l/\mathrm{d}t)}{H^2}[\mu_w l + \mu_n(L-l)] \tag{12}$$

where H and L are the width and length of the channel respectively, l is the advancing length of the wetting phase in the channel, θ_a is the advancing contact angle, μ_w and μ_n are the viscosity of the wetting phase and the non-wetting phase, respectively. Let $A = \mu_w - \mu_n$, $B = \mu_n L$, $C = H\sigma\cos\theta_a/6$, the Eq.(12) simplified as:

$$\frac{\mathrm{d}l}{\mathrm{d}t} = \frac{C}{Al + B} \tag{13}$$

304 A general solution of Eq.(13) is as follows by considering the initial length of the wetting
305 phase is zero.

$$\frac{1}{2}Al^2 + Bl = Ct \tag{14}$$

306 Let us consider two specific conditions. First, when the viscosity of the nonwetting phase
307 can be neglected compared to that of the wetting phase, i.e. $\mu_n = 0$ and $B = 0$, the Eq.(14)
308 simplified to the LW type equation as

$$l = \sqrt{\frac{2C}{A}t} \tag{15}$$

309 which indicates that the interface front position is proportional with $\sqrt{t}$. It is easy to understand
310 as that the driving capillary force keeps nearly constant but the resistant viscous force increases
311 along the SI process.

312 Secondly, when $\mu_w = \mu_n$ and $A = 0$, the Eq.(14) simplified to

$$l = \frac{C}{B}t \tag{16}$$

313 which indicates that the wetting phase propagates linearly with *t*. The mechanism behind the
314 linear behavior can be easily understood since the capillary driving force and total viscous
315 resistance force remain a constant during the process.

316 The improved multi-component SC-LBM was used to simulate the SI in a straight
317 channel. As illustrated in Figure 4(a), the calculation domain has a size of $N_x \times N_y \times N_z =$
318 $800 \times 1 \times 42$ lattices with the channel located on the right half of the model. The bounce-back
319 boundary condition was implemented on the channel walls and the periodic boundary condition
320 was implemented on the other boundaries. The wetting phase with a length of 400 lattices has 10
321 lattices overlap with the channel and the other fluid nodes were initialized with the non-wetting
322 phase. The β value was set as -0.22 to simulate a nearly completely wetting case. Three distinct
323 SI cases were simulated with viscosity ratios $\frac{\mu_w}{\mu_n} = 0.01, 1, \text{and } 100$. For the cases of $\frac{\mu_w}{\mu_n} =$
324 $0.01 \text{ and } 1$, the s_v^2 values were set equal to 1, and the s_v^1 were set equal to 1.98 and 1,
325 respectively. For the case of $\frac{\mu_w}{\mu_n} = 100$, the s_v^1 was set equal to 1, and the s_v^2 was set equal to
326 1.98. Comparison between the simulation and theoretical results are plotted in Figure 4(b), which
327 show good agreements. When $\frac{\mu_w}{\mu_n} = 0.01$, the imbibition showed an accelerating trend. When
328 $\frac{\mu_w}{\mu_n} = 1$, a linear trend was observed as indicated by Eq. (16). Moreover, the imbibition trend was
329 well described by the LW law, i.e. Eq. (15), when $\frac{\mu_w}{\mu_n} = 100$. These results validated the
330 improved multicomponent SC-LBM in simulation the SI with different fluid properties.
331

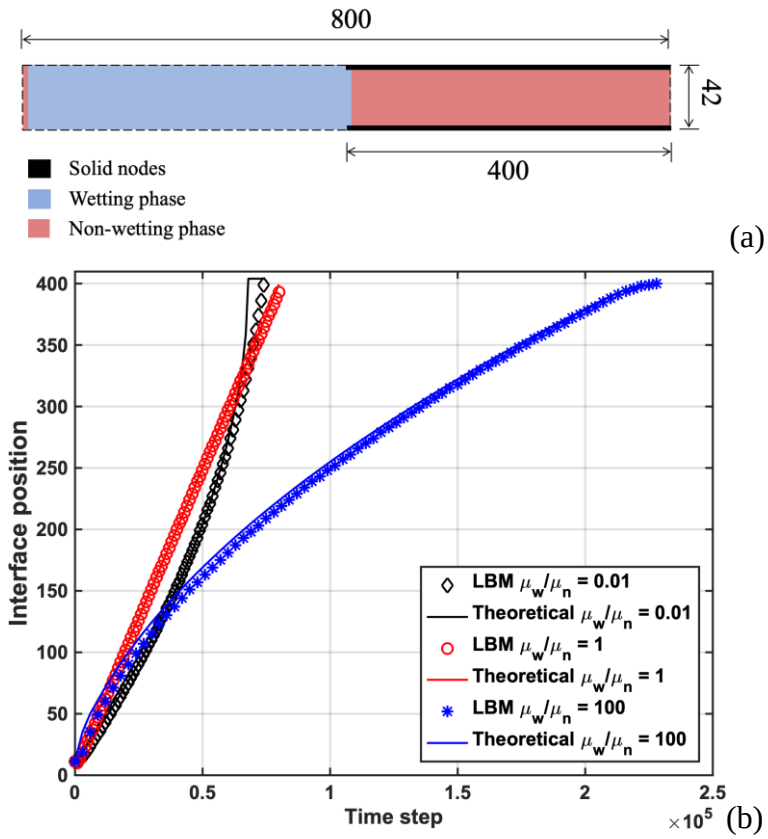

Figure. 4. Validation of three SI cases in a straight channel. (a) Illustration of the SI simulation model, (b) comparison of the front propagation between the simulated and theoretical results.

3 Results

The co-current SI behaviors in an actual 3D pore space, as shown in Figure 1(e), were simulated using the proposed multi-component SC-LBM under ambient and reservoir conditions, respectively. From here and after, the ambient condition represents that the temperature equals to 20 ℃ and pressure equals to 0.1 MPa. The reservoir condition represents that the temperature equals to 80 ℃ and pressure equals to 15 MPa. Comparisons of the SI behaviors under the two conditions were provided based on the simulation results.

343 ### 3.1 Model setup

344 In this work, we chose pure water and n-decane as representative aqueous and oil phases.
345 According to the data from the National Institute of Standard and Technology
346 (https://webbook.nist.gov/chemistry/), the viscosity of water at the ambient condition and
347 reservoir condition is 1.002 mPa·s and 0.358 mPa·s, respectively. The viscosity of n-decane at
348 the ambient condition and reservoir condition is 0.913 mPa·s and 0.523 mPa·s, respectively. As a
349 result, the viscosity ratio between the wetting phase and the non-wetting phase equals 1.097 at
350 ambient condition and 0.685 at reservoir condtion. The water and n-decane are far from their
351 critical point at both conditions. They were treated as conventional fluids rather than supercritical
352 fluids.

353 Numerous works have been performed to measure the surface tension of water-
354 hydrocarbon systems at different temperature and pressure conditions (Firoozabadi & Ramey,
355 1988; Georgiadis et al., 2011; McCaffery, 1972; S. Yang, 2017; Zeppieri et al., 2001). It was
356 found that the surface tension between water and pure liquid hydrocarbon decreased with the
357 temperature at a constant pressure. The change of surface tension with pressure could be
358 neglected in most cases. The surface tension between water and n-decane is around 52 mN/m at
359 ambient condition and 45 mN/m at reservoir condition according to the work of Georgiadis et al
360 (Georgiadis et al., 2011).

361 Moreover, it is found that temperature and pressure have little effect on the wettability of
362 the oil-bearing reservoir rock (S. Yang, 2017). Here, we considered the pore surface is
363 hydrophilic and the same wettability of the pore surface is set under the ambient and reservoir
364 conditions. Compared with the ambient condition, the high temperature and pressure under the
365 reservoir condition led to a smaller capillary force due to the slightly smaller surface tension as

366 well as a smaller viscous force due to the smaller viscosity. In other words, the driven force and
367 resistant force are both smaller under the reservoir condition than under the ambient condition.
368 Thus, the SI behavior in these two conditions needs to be further investigated.

369 To quantify the SI behavior in the representative porous model under ambient and
370 reservoir conditions, two parallel simulations were conducted with representative parameters for
371 the two conditions. The calculation domain has a size of $N_x \times N_y \times N_z = 150 \times 100 \times 100$
372 lattices, with the 100^3 size porous model located on the right of the domain. Initially, a 45 lattices
373 long wetting phase plug was set in the left of the porous model with 5 lattices overlap. The
374 bounce-back boundary condition was implemented on the solid nodes and the periodic boundary
375 condition was implemented on the other boundaries.

376 In our previous simulation of liquid-gas SI case, where the gas viscosity can be safely
377 ignored (Zheng, Ju, et al., 2018), we have shown an easy way to convert the lattice units into
378 physical units by the Buckingham π theorem. Here liquid-liquid SI cases were calculated and one
379 more Π term should be included, which can be chosen as the viscosity ratio between the wetting
380 phase and the non-wetting phase. In the simulation, the viscosity ratios between the wetting
381 phase and the non-wetting phase were set the same as that of the water and n-decane under the
382 two conditions. In addition, the percentage of surface tension decrease from ambient condition to
383 reservoir condition was also set according to that of the water and n-decane. Moreover, the pore
384 surface was set as hydrophilic with a contact angle of $7.67°$ at both ambient and reservoir
385 conditions. Parameters used in the two cases are list in Table 1.
386

Table 1. Parameters used in the SI simulation under ambient and reservoir conditions.

Cases	Ambient condition	Reservoir condition
ρ_B	0.97	
ρ_S	0.03	
β	-0.22	
θ	7.67°	
s_v^1	0.67	1.16
s_v^2	0.71	0.98
μ_v^1	0.33	0.12
μ_v^2	0.30	0.17
G	3.60	3.47
σ	0.073	0.063

3.2 SI behavior under ambient and reservoir conditions

The SI behaviors in the representative porous structure of tight sandstone were simulated with the above settings for ambient and reservoir conditions. In both cases, the wetting phase imbibed into the model from the left surface and drove the nonwetting phase out the model from the right surface. A total time step of 100,000 was calculated for both conditions.

The SI pattern at different time steps under ambient and reservoir conditions are shown in Figure 5(a) and (b) respectively. In general, the wetting phase imbibed quicker under the reservoir condition than the ambient condition. Part of the wetting phase front gradually reached to the right surface of the model under the reservoir condition, while none of the wetting phase fronts reached the right surface at the end of the 100,000 time step calculation. This was caused by the fact that the overall resistant viscous force under the reservoir condition was about half as much as that of the ambient condition, although the driving capillary force was slightly smaller.

The imbition front of the wetting phase showed a complex morphology, which was usually named interface front roughening (Gruener et al., 2012). This phenomenon mainly

occurred in high aspect ratio pores during the SI. Figure 6(a) shows the front tip positions of the wetting phase along with the SI for both conditions. In general, the front tip propagated faster under the reservoir condition and reached to the right surface at the time step of 48,000. Moreover, the front tip presented an irregular propagation pattern. Temporary stagnation of the front can be observed in both conditions, which occurred as the front meniscus propagating from the pore throat to the pore body.

Besides, we calculated the tail interface position of the wetting phase plug, as shown in Figure 6(b). The tail interface propagation under the reservoir condition was about two times as fast as that under the ambient condition. For the reservoir condition, the tail interface position of the wetting phase plug showed a slightly accelerating trend along with the time step because a lower viscosity wetting phase was displacing a relatively larger viscosity nonwetting phase.

Moreover, we calculated the oil recovery ratio in the porous model, as shown in Figure 6(c). As expected from the continuity hypothesis, the oil recovery ratio showed a very similar trend with the tail interface position. The oil recovery ratio reached 68.76% under the reservoir condition at the time step of T = 100,000.

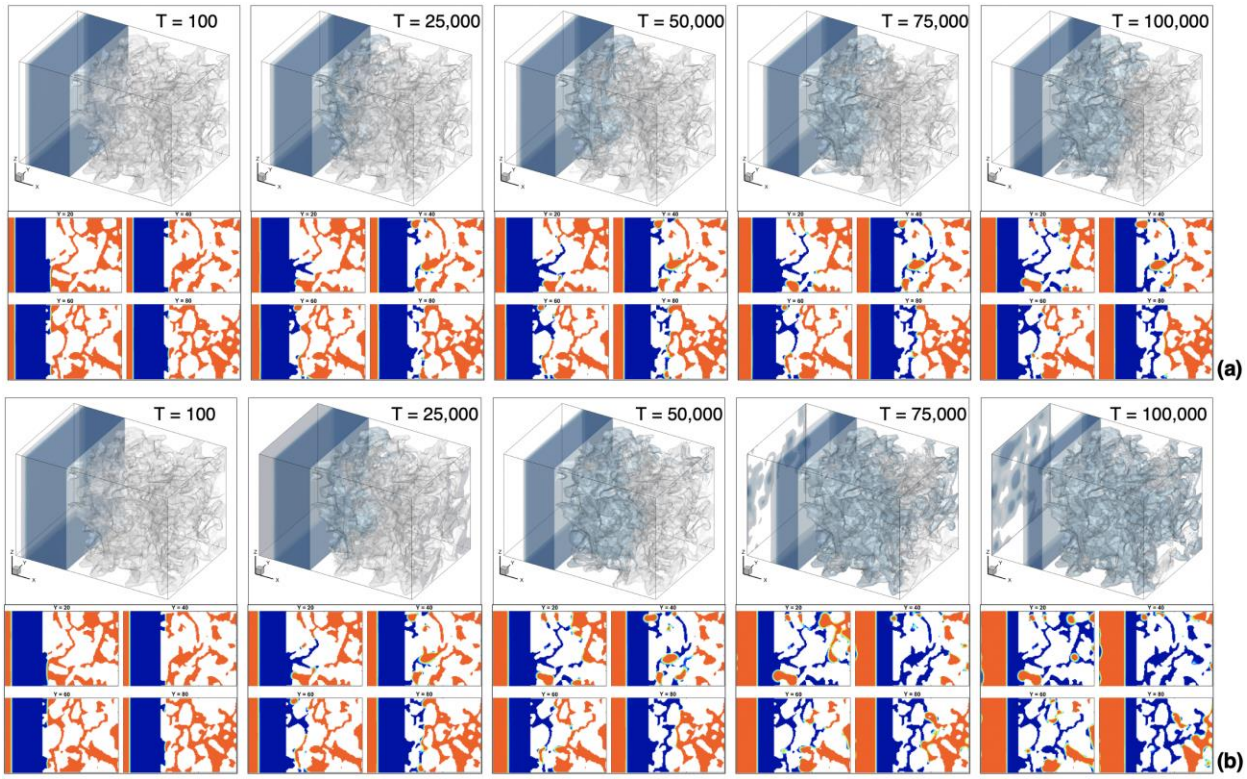

Figure. 5. Visualization of the SI behaviors in the representative porous model at the time steps of 100, 25,000, 50,000, 75,000, and 100,000. (a) Under the ambient condition, (b) under the reservoir condition. The upper row of each figure displays the 3D wetting phase morphology in the porous model, with the blue represents the water phase and the grey represents the pore space. The lower row displays the two phases distribution in the slices of Y=20, 40, 60, and 80 of the porous model with the blue represent the water phase and the red represent the oil phase.

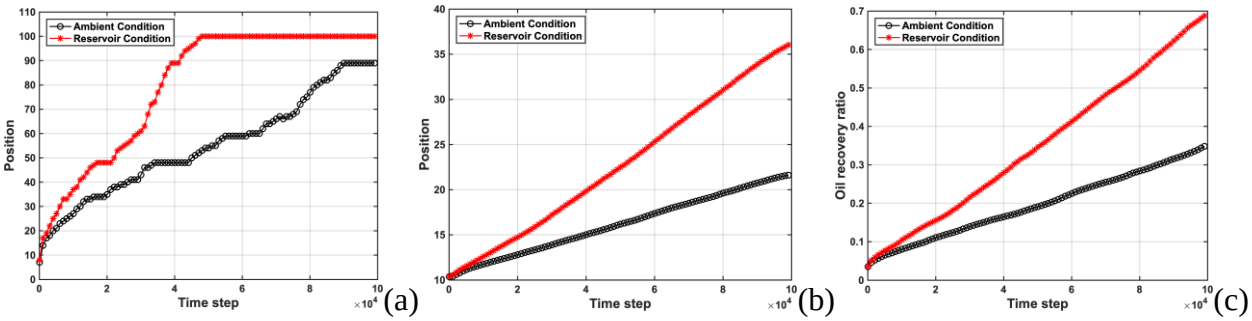

Figure. 6. Calculation of the SI pattern based on the simulation results. (a) Front tip position of the wetting phase, (b) tail interface position of the wetting phase plug, (c) oil recovery ratio in the porous model along with the SI.

3.3 Snap-off of the oil droplets

Snap-off of the oil droplets can be observed under both conditions, as shown in Figure 5(a) and (b), which usually happened in a pore body surrounded by slit-shaped pore throats. Such a snap-off behavior can hardly be captured by simplified models such as the capillary bundle model. To quantify the snap-off behavior during the SI, we calculated the volume ratio of the snap-off oil droplets along with the simulations. As shown in Figure 7(a), the occupied pore volume ratio of the snap-off oil droplets increased along with the SI. The curves showed jump increases when a new snap-off of the oil droplet occurred. A small decreasing trend of the curve can be observed after each jump. This was caused by the inherent compressibility effect of the SC-LBM. Due to the slower SI under the ambient condition, the snap-off oil droplet ratio showed a slower increasing trend. At the time step of T = 100,000, the snap-off of the oil droplet under the reservoir condition almost reached a stable state. The snap-off of the oil droplets accounted for parts of the trapped oil in an oil field. Moreover, these stuck oil droplets may block the transport channels and detrimental to further oil production.

In order to quantitatively characterize the snap-off of the oil droplet after the complete SI, we continuously calculated the SI in the porous structure under the reservoir condition. Further SI was observed in the model. At the time step around 146,000, the distribution of the water and oil phases reached an equilibrium and the SI nearly stopped in the porous model. As shown in Figure 7(b), the oil droplets mainly stuck in the pore body. We labeled the oil droplets in the pore space by image processing methods. As calculated, 18 oil droplets, whose volume was larger than 100 voxels, dispersed and stuck in the pore body. These oil droplets occupied 9.47 % of the pore space in the model and retarded the further flow therein due to the Jamin effect (Xu et al., 2019).

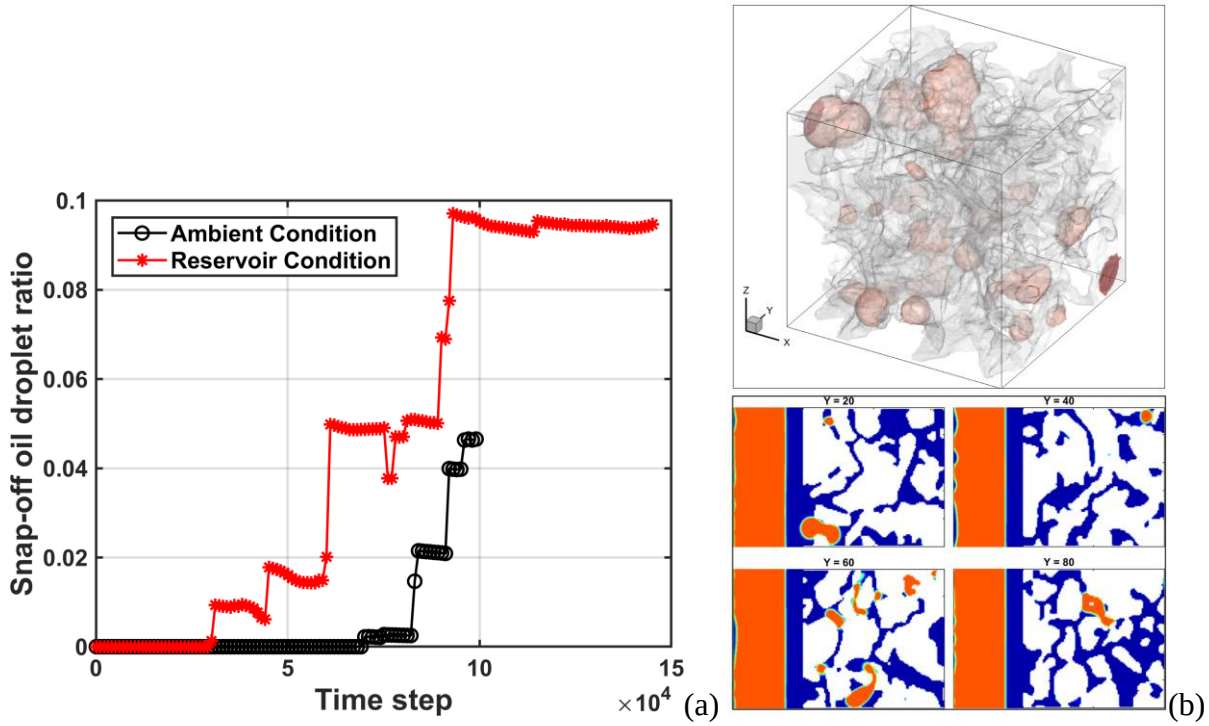

Figure. 7. Snap-off of the oil droplets during the SI. (a) Occupied pore volume ratio of the snap-off oil droplet along with the SI. (b) Final distribution of the water and oil phases in the porous model under the reservoir condition. The upper row displays the oil droplet in the porous model, with the red represent the oil droplet and the grey represent the pore space. The lower row displays the two-phase distribution in the slices of Y = 20, 40, 60, and 80 of the porous model with the blue represents the water phase and the red represents the oil phase.

4 Conclusions

An improved multi-component SC-LBM was developed with the modification of interaction force between the fluid and solid nodes. Good agreement between the simulation and theoretical results of different viscosity ratio SI cases in a straight channel demonstrated the ability of the proposed method in simulating the SI under various conditions. We employed the proposed method to simulate the SI behavior in a representative porous model under the ambient and reservoir conditions. Comparison of the SI in the same porous model showed that the imbibition of the wetting phase under the reservoir condition is about two times as fast as that under the ambient condition. The main reason caused the faster SI under the reservoir condition is the lower overall resistant viscous force. Besides, the snap-off of the oil droplets during the SI

mainly occurred in a pore body surrounded by slit-shaped pore throats. The snap-off caused the oil droplets stuck in the pore space. At the end of the SI process under the reservoir condition, dispersed and stuck oil droplets accounted for 9.47 % of the pore volume. The distinct SI behavior under the ambient and reservoir condition suggested that the laboratory SI data, which usually obtained under ambient condition should be carefully applied in interpreting the underground cases. Moreover, the snap-off of the oil droplet in the complex pore space indicated that the simplification of the pore space into simple geometries would cause a discrepancy in predicting the SI behavior in complex pore structures, especially those with high aspect ratio.

Acknowledgments

The authors acknowledge financial support from the National Natural Science Foundation of China [No. 51904307, 51727807], the Fundamental Research Funds for the Central Universities (00/8000150A137), the Undergraduate Training Program for Innovation of State Key Laboratory of Coal Resources and Safe Mining (SKLCRSM20DC16), and the Innovation Teams of the Ten-Thousand Talents Program sponsored by the Ministry of Science and Technology of China [2016RA4067].

Data Availability statement

The data for this paper can be obtained from https://figshare.com/s/0c9e5de9f7484728c75c.

References

Abbasi, M. A., Ezulike, D. O., Dehghanpour, H., & Hawkes, R. V. (2014). A comparative study of flowback rate and pressure transient behavior in multifractured horizontal wells completed in tight gas and oil reservoirs. *Journal of Natural Gas Science and Engineering, 17*, 82-93. doi:10.1016/j.jngse.2013.12.007

Aidun, C. K., & Clausen, J. R. (2010). Lattice-Boltzmann Method for Complex Flows. *Annual Review of Fluid Mechanics, 42*(1), 439-472. doi:10.1146/annurev-fluid-121108-145519

Alhammadi, A. M., Gao, Y., Akai, T., Blunt, M. J., & Bijeljic, B. (2020). Pore-scale X-ray imaging with measurement of relative permeability, capillary pressure and oil recovery in a mixed-wet micro-porous carbonate reservoir rock. *Fuel, 268*, 117018. doi:10.1016/j.fuel.2020.117018

AlRatrout, A., Blunt, M. J., & Bijeljic, B. (2018). Wettability in complex porous materials, the mixed-wet state, and its relationship to surface roughness. *Proceedings of the National Academy of Sciences, 115*(36), 8901-8906. doi:10.1073/pnas.1803734115

Alzahid, Y. A., Aborshaid, H., Asali, M., McClure, J., Chen, C., Mostaghimi, P., . . . Armstrong, R. T. (2020). Real-time synchrotron-based X-ray computed microtomography during in situ emulsification. *Journal Of Petroleum Science and Engineering, 195*, 107885. doi:10.1016/j.petrol.2020.107885

Armstrong, R. T., Georgiadis, A., Ott, H., Klemin, D., & Berg, S. (2014). Critical capillary number: Desaturation studied with fast X-ray computed microtomography. *Geophysical Research Letters, 41*(1), 55-60. doi:10.1002/2013gl058075

Ashraf, S., Visavale, G., Bahga, S. S., & Phirani, J. (2017). Spontaneous imbibition in parallel layers of packed beads. *The European Physical Journal E, 40*(4), 39. doi:10.1140/epje/i2017-11530-8

Bakhshian, S., Murakami, M., Hosseini, S. A., & Kang, Q. (2020). Scaling of Imbibition Front Dynamics in Heterogeneous Porous Media. *Geophysical Research Letters, 47*(14), e2020GL087914. doi:10.1029/2020gl087914

Bazaikin, Y., Gurevich, B., Iglauer, S., Khachkova, T., Kolyukhin, D., Lebedev, M., . . . Reshetova, G. (2017). Effect of CT image size and resolution on the accuracy of rock property estimates. *Journal of Geophysical Research: Solid Earth, 122*(5), 3635-3647. doi:10.1002/2016JB013575

Bertoncello, A., Wallace, J., Blyton, C., Honarpour, M., & Kabir, C. S. (2014). Imbibition and Water Blockage In Unconventional Reservoirs: Well-Management Implications During Flowback and Early Production. *Spe Reservoir Evaluation & Engineering, 17*(4), 497-506. doi:10.2118/167698-ms

Blunt, M. J., Bijeljic, B., Dong, H., Gharbi, O., Iglauer, S., Mostaghimi, P., . . . Pentland, C. (2013). Pore-scale imaging and modelling. *Advances In Water Resources, 51*(0), 197-216. doi:10.1016/j.advwatres.2012.03.003

Buades, A., Coll, B., & Morel, J.-M. (2005). *A non-local algorithm for image denoising.* Paper presented at the IEEE Computer Society Conference on Computer Vision and Pattern Recognition (CVPR'05), San Diego, CA, USA.

Cai, J., Jin, T., Kou, J., Zou, S., Xiao, J., & Meng, Q. (2021). Lucas–Washburn Equation-Based Modeling of Capillary-Driven Flow in Porous Systems. *Langmuir*. doi:10.1021/acs.langmuir.0c03134

Chen, L., Kang, Q., Mu, Y., He, Y. L., & Tao, W. Q. (2014). A critical review of the pseudopotential multiphase lattice Boltzmann model: Methods and applications. *International Journal of Heat & Mass Transfer, 76*(6), 210-236. doi:10.1016/j.ijheatmasstransfer.2014.04.032

Chen, S., & Gary, D. D. (1998). Lattice Boltzmann method for fluid flows. *Annual Review of Fluid Mechanics, 30*(1), 329-364. doi:10.1146/annurev.fluid.30.1.329

Chen, Z., Elsworth, D., & Wang, M. (2020). Does Low-Viscosity Fracturing Fluid Always Create Complex Fractures? *Journal of Geophysical Research: Solid Earth, 125*(9). doi:10.1029/2020jb020332

Cheng, Z., Wang, Q., Ning, Z., Li, M., Lyu, C., Huang, L., & Wu, X. (2018). Experimental Investigation of Countercurrent Spontaneous Imbibition in Tight Sandstone Using Nuclear Magnetic Resonance. *Energy & Fuels, 32*(6), 6507-6517. doi:10.1021/acs.energyfuels.8b00394

Coon, E. T., Porter, M. L., & Kang, Q. (2014). Taxila LBM: a parallel, modular lattice Boltzmann framework for simulating pore-scale flow in porous media. *Computational Geosciences, 18*(1), 17-27. doi:10.1007/s10596-013-9379-6

d'Humières, D. (2002). Multiple–relaxation–time lattice Boltzmann models in three dimensions. *Philosophical Transactions of the Royal Society of London. Series A: Mathematical, Physical and Engineering Sciences, 360*(1792), 437-451. doi:10.1098/rsta.2001.0955

Dai, C., Wang, X., Li, Y., Lv, W., Zou, C., Gao, M., & Zhao, M. (2017). Spontaneous Imbibition Investigation of Self-Dispersing Silica Nanofluids for Enhanced Oil Recovery in Low-Permeability Cores. *Energy & Fuels, 31*(3). doi:10.1021/acs.energyfuels.6b03244

David, C., Menéndez, B., & Mengus, J. M. (2011). X-ray imaging of water motion during capillary imbibition: Geometry and kinetics of water front in intact and damaged porous rocks. *Journal of Geophysical Research: Solid Earth, 116*(B3), n/a-n/a. doi:10.1029/2010JB007972

De Maio, A., Palpacelli, S., & Succi, S. (2011). A New Boundary Condition for Three-Dimensional Lattice Boltzmann Simulations of Capillary Filling in Rough Micro-Channels. *Communications in Computational Physics, 9*(5), 1284-1292. doi:10.4208/cicp.141009.241110s

Dong, H., & Blunt, M. J. (2009). Pore-network extraction from micro-computerized-tomography images. *Physical Review E, 80*(3), 036307. doi:10.1103/PhysRevE.80.036307

Fernø, M. A., Haugen, Å., Wickramathilaka, S., Howard, J., Graue, A., Mason, G., & Morrow, N. R. (2013). Magnetic resonance imaging of the development of fronts during spontaneous imbibition. *Journal Of Petroleum Science and Engineering, 101*, 1-11. doi:10.1016/j.petrol.2012.11.012

Firoozabadi, A., & Ramey, H. J., Jr. (1988). Surface Tension Of Water-Hydrocarbon Systems At Reservoir Conditions. *Journal Of Canadian Petroleum Technology, 27*(03), 9. doi:10.2118/88-03-03

Fries, N., & Dreyer, M. (2009). Dimensionless scaling methods for capillary rise. *Journal Of Colloid and Interface Science, 338*(2), 514-518. doi:10.1016/j.jcis.2009.06.036

Gao, Y., Raeini, A. Q., Selem, A. M., Bondino, I., Blunt, M. J., & Bijeljic, B. (2020). Pore-scale imaging with measurement of relative permeability and capillary pressure on the same reservoir sandstone sample under water-wet and mixed-wet conditions. *Advances In Water Resources*, 103786. doi:10.1016/j.advwatres.2020.103786

Georgiadis, A., Maitland, G., Trusler, J. P. M., & Bismarck, A. (2011). Interfacial Tension Measurements of the (H2O + n-Decane + CO2) Ternary System at Elevated Pressures and Temperatures. *Journal of Chemical & Engineering Data, 56*(12), 4900-4908. doi:10.1021/je200825j

Gruener, S., Sadjadi, Z., Hermes, H. E., Kityk, A. V., Knorr, K., Egelhaaf, S. U., . . . Huber, P. (2012). Anomalous front broadening during spontaneous imbibition in a matrix with elongated pores. *Proceedings of the National Academy of Sciences, 109*(26), 10245-10250. doi:10.1073/pnas.1119352109

Habibi, A., Xu, M., Dehghanpour, H., Bryan, D., & Uswak, G. (2015). *Understanding Rock-Fluid Interactions in the Montney Tight Oil Play*. Paper presented at the SPE/CSUR Unconventional Resources Conference, Calgary, Alberta, Canada.

Hatiboglu, C. U., & Babadagli, T. (2008). Pore-scale studies of spontaneous imbibition into oil-saturated porous media. *Physical Review E, 77*(6), 066311. doi:10.1103/physreve.77.066311

Haugen, Å., Fernø, M. A., Mason, G., & Morrow, N. R. (2014). Capillary pressure and relative permeability estimated from a single spontaneous imbibition test. *Journal Of Petroleum Science and Engineering, 115*, 66-77. doi:10.1016/j.petrol.2014.02.001

Hodder, K. J., & Nychka, J. A. (2019). Silane Treatment of 3D-Printed Sandstone Models for Improved Spontaneous Imbibition of Water. *Transport In Porous Media, 129*(2), 583-598. doi:10.1007/s11242-018-1134-y

Huang, H., Thorne, D. T., Schaap, M. G., & Sukop, M. C. (2007). Proposed approximation for contact angles in Shan-and-Chen-type multicomponent multiphase lattice Boltzmann models. *Physical Review E, 76*(76), 75-80. doi:10.1103/physreve.76.066701

Iglauer, S., & Lebedev, M. (2018). High pressure-elevated temperature x-ray micro-computed tomography for subsurface applications. *Adv Colloid Interface Sci, 256*, 393-410. doi:10.1016/j.cis.2017.12.009

Jafari, I., Masihi, M., & Zarandi, M. N. (2017). Numerical simulation of counter-current spontaneous imbibition in water-wet fractured porous media: Influences of water injection velocity, fracture aperture, and grains geometry. *Physics Of Fluids, 29*(11), 113305. doi:10.1063/1.4999999

Joyce, S., L., U. J., Steffen, B., & Holger, O. (2015). Nanoscale imaging of pore-scale fluid-fluid-solid contacts in sandstone. *Geophysical Research Letters, 42*(7), 2189-2195. doi:doi:10.1002/2015GL063354

Ju, Y., Gong, W., Chang, W., & Sun, M. (2020). Effects of pore characteristics on water-oil two-phase displacement in non-homogeneous pore structures: A pore-scale lattice Boltzmann model considering various fluid density ratios. *International Journal of Engineering Science, 154*, 103343. doi:10.1016/j.ijengsci.2020.103343

Ju, Y., Xi, C., Zhang, Y., Mao, L., Gao, F., & Xie, H. (2018). Laboratory In Situ CT Observation of the Evolution of 3D Fracture Networks in Coal Subjected to Confining Pressures and Axial Compressive Loads: A Novel Approach. *Rock Mechanics and Rock Engineering*, 1-15. doi:10.1007/s00603-018-1459-4

Kalantari Meybodi, M., Daryasafar, A., & Karimi, M. (2016). Determination of hydrocarbon-water interfacial tension using a new empirical correlation. *Fluid Phase Equilibria, 415*, 42-50. doi:10.1016/j.fluid.2016.01.037

Kamali, M. R., Gillissen, J. J. J., Sundaresan, S., & Van den Akker, H. E. A. (2011). Contact line motion without slip in lattice Boltzmann simulations. *Chemical Engineering Science, 66*(14), 3452-3458. doi:10.1016/j.ces.2011.04.010

Kibria, M. G., Hu, Q. H., Liu, H., Zhang, Y. X., & Kang, J. H. (2018). Pore structure, wettability, and spontaneous imbibition of Woodford Shale, Permian Basin, West Texas. *Marine and Petroleum Geology, 91*, 735-748. doi:10.1016/j.marpetgeo.2018.02.001

Kuang, W., Saraji, S., & Piri, M. (2020). Nanofluid-Induced Wettability Gradient and Imbibition Enhancement in Natural Porous Media: A Pore-scale Experimental Investigation. *Transport In Porous Media*. doi:10.1007/s11242-020-01459-0

Lai, J., Wang, G., Wang, Z., Chen, J., Pang, X., Wang, S., . . . Fan, X. (2018). A review on pore structure characterization in tight sandstones. *Earth-Science Reviews, 177*, 436-457. doi:10.1016/j.earscirev.2017.12.003

Lan, Q., Xu, M., Binazadeh, M., Dehghanpour, H., & Wood, J. M. (2015). A comparative investigation of shale wettability: The significance of pore connectivity. *Journal of Natural Gas Science and Engineering, 27*, 1174-1188. doi:10.1016/j.jngse.2015.09.064

Li, Q., Luo, K. H., Kang, Q. J., He, Y. L., Chen, Q., & Liu, Q. (2016). Lattice Boltzmann methods for multiphase flow and phase-change heat transfer. *Progress in Energy & Combustion Science, 52*, 62-105. doi:10.1016/j.pecs.2015.10.001

Liu, H., & Zhang, Y. (2016). Lattice Boltzmann simulation of the trapping of a microdroplet in a well of surface energy. *Computers & Fluids*. doi:10.1016/j.compfluid.2016.10.031

Liu, J., Sheng, J. J., & Huang, W. (2019). Experimental Investigation of Microscopic Mechanisms of Surfactant-Enhanced Spontaneous Imbibition in Shale Cores. *Energy & Fuels*. doi:10.1021/acs.energyfuels.9b01324

Liu, Y., Cai, J., Sahimi, M., & Qin, C. (2020). A Study of the Role of Microfractures in Counter-Current Spontaneous Imbibition by Lattice Boltzmann Simulation. *Transport In Porous Media*. doi:10.1007/s11242-020-01425-w

McCaffery, F. G. (1972). Measurement of Interfacial Tensions And Contact Angles At High Temperature And Pressure. *Journal Of Canadian Petroleum Technology, 11*(03), 8. doi:10.2118/72-03-03

Meng, Q., Liu, H., Wang, J., & Zhang, H. (2016). Effect of Wetting-Phase Viscosity on Cocurrent Spontaneous Imbibition. *Energy & Fuels, 30*(2), 835-843. doi:10.1021/acs.energyfuels.5b02321

Mohammadi, S., Kord, S., & Moghadasi, J. (2019). An experimental investigation into the spontaneous imbibition of surfactant assisted low salinity water in carbonate rocks. *Fuel, 243*, 142-154. doi:10.1016/j.fuel.2019.01.074

Nelson, P. H. (2009). Pore-throat sizes in sandstones, tight sandstones, and shales. *AAPG Bulletin, 93*(3), 329-340. doi:10.1306/10240808059

Ponomarenko, A., Quéré, D., & Clanet, C. (2011). A universal law for capillary rise in corners. *Journal Of Fluid Mechanics, 666*, 146-154. doi:10.1017/s0022112010005276

Porter, M. L., Coon, E. T., Kang, Q., Moulton, J. D., & Carey, J. W. (2012). Multicomponent interparticle-potential lattice Boltzmann model for fluids with large viscosity ratios. *Physical Review E, 86*(3), 036701. doi:10.1103/PhysRevE.86.036701

Primkulov, B. K., Chui, J. Y. Y., Pahlavan, A. A., Macminn, C. W., & Juanes, R. (2020). Characterizing Dissipation in Fluid-Fluid Displacement Using Constant-Rate Spontaneous Imbibition. *Physical Review Letters, 125*(17). doi:10.1103/physrevlett.125.174503

Reyssat, M., Courbin, L., Reyssat, E., & Stone, H. A. (2008). Imbibition in geometries with axial variations. *Journal Of Fluid Mechanics, 615*(9), 335-344. doi:10.1017/s0022112008003996

Singh, H. (2016). A critical review of water uptake by shales. *Journal of Natural Gas Science and Engineering, 34*, 751-766. doi:10.1016/j.jngse.2016.07.003

Singh, K., Jung, M., Brinkmann, M., & Seemann, R. (2019). Capillary-Dominated Fluid Displacement in Porous Media. *Annual Review of Fluid Mechanics, 51*, 429-449. doi:10.1146/annurev-fluid-010518-040342

Singh, K., Menke, H., Andrew, M., Lin, Q., Rau, C., Blunt, M. J., & Bijeljic, B. (2017). Dynamics of snap-off and pore-filling events during two-phase fluid flow in permeable media. *Scientific Reports, 7*(1), 5192. doi:10.1038/s41598-017-05204-4

Strand, S., Puntervold, T., & Austad, T. (2008). Effect of Temperature on Enhanced Oil Recovery from Mixed-Wet Chalk Cores by Spontaneous Imbibition and Forced Displacement Using Seawater. *Energy & Fuels, 22*(5), 3222-3225. doi:10.1021/ef800244v

Sun, Y., Kharaghani, A., & Tsotsas, E. (2016). Micro-model experiments and pore network simulations of liquid imbibition in porous media. *Chemical Engineering Science, 150*, 41-53. doi:10.1016/j.ces.2016.04.055

Valvatne, P. H., & Blunt, M. J. (2004). Predictive pore-scale modeling of two-phase flow in mixed wet media. *Water Resources Research, 40*(7), 187-187. doi:10.1029/2003wr002627

Voorn, M., Exner, U., & Rath, A. (2013). Multiscale Hessian fracture filtering for the enhancement and segmentation of narrow fractures in 3D image data. *Computers & Geosciences, 57*, 44-53. doi:10.1016/j.cageo.2013.03.006

Wang, X. Z., Peng, X. L., Zhang, S. J., Du, Z. W., & Zeng, F. H. (2018). Characteristics of oil distributions in forced and spontaneous imbibition of tight oil reservoir. *Fuel, 224*, 280-288. doi:10.1016/j.fuel.2018.03.104

Washburn, E. W. (1921). The Dynamics of Capillary Flow. *Physical Review, 17*(3), 273-283. doi:10.1103/physrev.17.273

Wu, Y., Gui, N., Yang, X., Tu, J., & Jiang, S. (2018). Improved stability strategies for pseudo-potential models of lattice Boltzmann simulation of multiphase flow. *International Journal Of Heat and Mass Transfer, 125*, 66-81. doi:10.1016/j.ijheatmasstransfer.2018.04.021

Xie, C., Lei, W., Balhoff, M. T., Wang, M., & Chen, S. (2021). Self-adaptive preferential flow control using displacing fluid with dispersed polymers in heterogeneous porous media. *Journal Of Fluid Mechanics, 906*, A10. doi:10.1017/jfm.2020.763

Xu, D., Bai, B., Wu, H., Hou, J., Meng, Z., Sun, R., . . . Kang, W. (2019). Mechanisms of imbibition enhanced oil recovery in low permeability reservoirs: Effect of IFT reduction and wettability alteration. *Fuel, 244*, 110-119. doi:10.1016/j.fuel.2019.01.118

Yang, R., Guo, X., Yi, J., Fang, Z., Hu, Q., & He, S. (2017). Spontaneous Imbibition of Three Leading Shale Formations in the Middle Yangtze Platform, South China. *Energy & Fuels, 31*(7), 6903-6916. doi:10.1021/acs.energyfuels.7b00843

Yang, S. (2017). Interfacial Phenomena and Wettability of Reservoir Rocks. In *Fundamentals of Petrophysics* (pp. 317-363). Berlin, Heidelberg: Springer Berlin Heidelberg.

Zacharoudiou, I., Chapman, E. M., Boek, E. S., & Crawshaw, J. P. (2017). Pore-filling events in single junction micro-models with corresponding lattice Boltzmann simulations. *Journal Of Fluid Mechanics, 824*, 550-573. doi:10.1017/jfm.2017.363

Zeppieri, S., Rodríguez, J., & López de Ramos, A. L. (2001). Interfacial Tension of Alkane + Water Systems. *Journal of Chemical & Engineering Data, 46*(5), 1086-1088. doi:10.1021/je000245r

Zhang, C., Oostrom, M., Wietsma, T. W., Grate, J. W., & Warner, M. G. (2011). Influence of viscous and capillary forces on immiscible fluid displacement: Pore-scale experimental study in a water-wet micromodel demonstrating viscous and capillary fingering. *Energy & Fuels, 25*(8), 3493-3505. doi:10.1021/ef101732k

Zhao, B., MacMinn, C. W., & Juanes, R. (2016). Wettability control on multiphase flow in patterned microfluidics. *Proceedings of the National Academy of Sciences, 113*(37), 10251-10256. doi:10.1073/pnas.1603387113

Zhao, Y., Xue, S., Han, S., Chen, Z., Liu, S., Elsworth, D., . . . Chen, D. (2017). Effects of microstructure on water imbibition in sandstones using X-ray computed tomography and neutron radiography. *Journal of Geophysical Research: Solid Earth, 122*(7), 4963-4981. doi:10.1002/2016JB013786

Zheng, J., Chen, Z., Xie, C., Wang, Z., Lei, Z., Ju, Y., & Wang, M. (2018). Characterization of spontaneous imbibition dynamics in irregular channels by mesoscopic modeling. *Computers & Fluids, 168*, 21-31. doi:10.1016/j.compfluid.2018.01.024

Zheng, J., Ju, Y., & Wang, M. (2018). Pore-Scale Modeling of Spontaneous Imbibition Behavior in a Complex Shale Porous Structure by Pseudopotential Lattice Boltzmann Method. *Journal of Geophysical Research: Solid Earth, 123*(11), 9586-9600. doi:10.1029/2018jb016430

Zheng, J., Wang, Z., Ju, Y., Tian, Y., Jin, Y., & Chang, W. (2021). Visualization of water channeling and displacement diversion by polymer gel treatment in 3D printed heterogeneous porous media. *Journal Of Petroleum Science and Engineering, 198*, 108238. doi:10.1016/j.petrol.2020.108238